DRINet for Medical Image Segmentation

Liang Chen, Paul Bentley, Kensaku Mori, Kazunari Misawa,
Michitaka Fujiwara, and Daniel Rueckert, *Fellow, IEEE*

Abstract—Convolutional neural networks (CNNs) have revolutionized medical image analysis over the past few years. The U-Net architecture is one of the most well-known CNN architectures for semantic segmentation and has achieved remarkable successes in many different medical image segmentation applications. The U-Net architecture consists of standard convolution layers, pooling layers, and upsampling layers. These convolution layers learn representative features of input images and construct segmentations based on the features. However, the features learned by standard convolution layers are not distinctive when the differences among different categories are subtle in terms of intensity, location, shape, and size. In this paper, we propose a novel CNN architecture, called Dense-Res-Inception Net (DRINet), which addresses this challenging problem. The proposed DRINet consists of three blocks, namely a convolutional block with dense connections, a deconvolutional block with residual inception modules, and an unpooling block. Our proposed architecture outperforms the U-Net in three different challenging applications, namely multi-class segmentation of cerebrospinal fluid on brain CT images, multi-organ segmentation on abdominal CT images, and multi-class brain tumor segmentation on MR images.

Index Terms—Convolutional neural network, medical image segmentation, brain atrophy, abdominal organ segmentation.

I. INTRODUCTION

SIGNIFICANT progress has been achieved in the field of medical image analysis in recent years due to the advent of CNNs [1]. Within medical imaging, the problem of image segmentation has been one of the major challenges. Segmentation is a pre-requisite for many different types of clinical applications, including brain segmentation [2], cardiac ventricle segmentation [3], abdominal organ segmentation [4], and cell segmentation in biological images [5]. In these applications, the results of the segmentation are usually used to derive quantitative measurements or biomarkers for subsequent diagnosis and treatment planning.

Among the different approaches that use CNNs for medical image segmentation, the U-Net architecture [5] and its 3D extension [6] are widely used because of their flexible architectures. In the first part of the U-Net architecture (analysis path), deep features are learned while the second part of the U-Net architecture (synthesis path) performs segmentation based on these learned features. Training the two parts of the network in an end-to-end fashion yields good segmentation results. As the number of features in the first part of network is reduced because of convolutions and poolings, skip connections are used to allow dense feature maps from the analysis path to propagate to the corresponding layers in the synthesis part of the network, which improves the performance significantly.

However, the limitation of the U-Net architecture is its scalability. Specifically, deeper networks learn more representative features and result in better performance. Adding more layers to the network enlarges the parameter space, which allows the network to learn more representative features. However, this also increases the difficulties in training the network because gradients are likely to vanish during training. Therefore, the challenge is to make the network wider and deeper without gradient vanishing.

In computer vision, the state-of-the-art CNN architectures include the densely connected convolutional network (DenseNet) [7], [8] and the Inception-ResNet [9]. The DenseNet approach consists of a number of dense blocks with pooling layers between them to reduce the size of the feature maps. Within each dense block, layers are directly connected with all of their preceding layers, which is implemented via concatenation of feature maps in subsequent layers. This dense architecture has a number of advantages: Firstly, the concatenation of feature maps enables deep supervision so that gradients are propagated more easily to preceding layers, which makes the network training easier. Secondly, bottleneck layers (convolution layers with 1-by-1 kernels) are used to control the growth rate of parameters in the network. Finally, in the DenseNet architecture the final classifier uses features from all layers (instead of only features from the last layer as in standard CNN approaches), leading to improved classification performance.
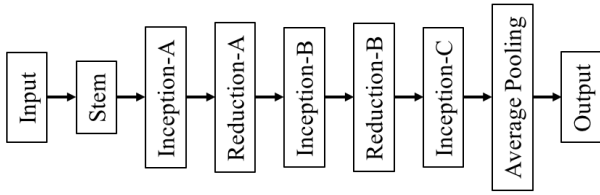
Fig. 1. The overall schema of the Inception-ResNet [9]. The whole architecture consists of some Inception and Reduction blocks. Each block contains a number of modules. The detailed structures in different blocks vary slightly.

The Inception network [10] is a CNN architecture which uses the Inception modules and allows for very deep networks. The main purpose of the Inception modules are: 1) to increase the depth and width of networks without adding more parameters; and 2) to achieve multi-scale features for processing. These are achieved by carefully designing structures of the Inception modules. The latest version of the Inception architecture [9] also uses residual connections, i.e. Inception-ResNet. Fig. 1 shows an overview of the Inception-ResNet: a stem convolution block, stacks of inception and reduction blocks, and the classifier. The stem block consists of a number of standard convolution and pooling layers, reducing the size of feature maps in lower layers (the ones close to the input). This aims to be memory efficient in training but is not strictly necessary. Each inception block consists of number of inception modules. The reduction blocks are inception modules with dimension reduction. An inception module consists of a number of branches of convolution layers. In each branch, a bottleneck layer reduces the number of feature maps. The feature maps are then processed by convolution layers with different sizes of kernels in different branches. The output of all branches are finally aggregated as the output of the inception module.

Inspired by the DenseNet and the Inception-ResNet, we propose an architecture consisting of dense connection blocks, residual Inception blocks, and unpooling blocks. We term this architecture Dense-Res-Inception Net (DRINet). We apply the proposed DRINet architecture for three challenging clinical segmentation problems, namely multi-class segmentation of brain CSF in CT images, abdominal multi-organ segmentation in CT images, and brain tumor segmentation (BraTS) in multi-modal MR images. The former two problems are based on clinical datasets while the last one is based on a publically benchmark dataset. Our main contributions are: 1) a novel combination of the dense connections with the inception structure to address segmentation problems. The use of dense connection blocks, residual inception blocks, and the unpooling blocks achieve high performance while maintaining computational efficiency; 2) easy and flexible implementation of the proposed network architecture; 3) state-of-the-art segmentation performance for challenging image segmentation tasks.

II. RELATED WORK

The basic CNN architecture for many semantic segmentation problems is the fully convolutional network (FCN), shown

in Fig. 2(a), which consists of cascaded convolution, pooling, and deconvolution layers. Convolution and pooling layers form the analysis path while the convolution and deconvolution layers form the synthesis path. The analysis path and the synthesis path are usually symmetric.

The U-Net (Fig. 2(b)) is the FCN with skip layers between layers in analysis path and synthesis path. The skip layers are implemented via concatenations and they allow deep supervision for the network. As such, the errors can propagate easily through the network. Therefore, the skip layers improve the network performance. In addition, residual connections can be used in the U-Net, which results in the Res-U-Net (Fig. 2(c)). In the Res-U-Net, the residual learning is implemented using the bottleneck building blocks with residual connections, which were used in the ResNet-50/101/152 architectures [11].

The DeepLab approach [12] involved atrous convolutions and poolings within the CNN architecture to solve segmentation problems, as well as conditional random field (CRF) models for post processing. Based on the DeepLab architecture, Chen et al. [13] proposed the latest DeepLabV3 architecture. In DeepLabV3, a simple synthesis path is used. This synthesis path only consists of very few convolution layers, which is different from the synthesis path used in the FCN and the U-Net architectures. Skip connections are used to connect the analysis path and the synthesis path.

The DenseNet was extended in a fully convolutional fashion so that it can be used for segmentation tasks [14]. Specifically, an upsampling transition module was proposed in correspondence to the downsampling transition module in the original DenseNet. In addition, the macro-architecture of the fully convolutional DenseNet is similar to the U-Net where skip connections are used.

Finally, the Pyramid Scene Parsing Network (PSPNet) [15] was proposed to solve the challenging scene parsing problem. In the scene parsing problem, prior knowledge could be incorporated in CNNs to improve performance. For example, cars are likely to be on the road while they should not be in the sky. Global context is required to incorporate these priors. The pyramid pooling module in the PSPNet investigate features in multiple levels, achieving the state-of-the-art performance.

III. DRINET

A. Overview

Fig. 2(d) demonstrates our proposed DRINet architecture. Similar to the FCN, the DRINet has an analysis path and a synthesis path. Stacks of dense connection blocks, instead of standard convolution layers make up the analysis path, which is inspired by the DenseNet. The synthesis path consists of residual inception blocks and unpooling blocks, which are inspired by the Res-Inception Net. To be more efficient in terms of memory, the DRINet has no skip connections.

B. Dense Connection Block

We employ convolutional dense connection blocks [7] in the analysis path, which are shown in Fig. 3. Formally, let us assume x_l is the output of the lth layer and $f(\cdot)$ is a convolution function followed by batch normalization (BN) [16] and
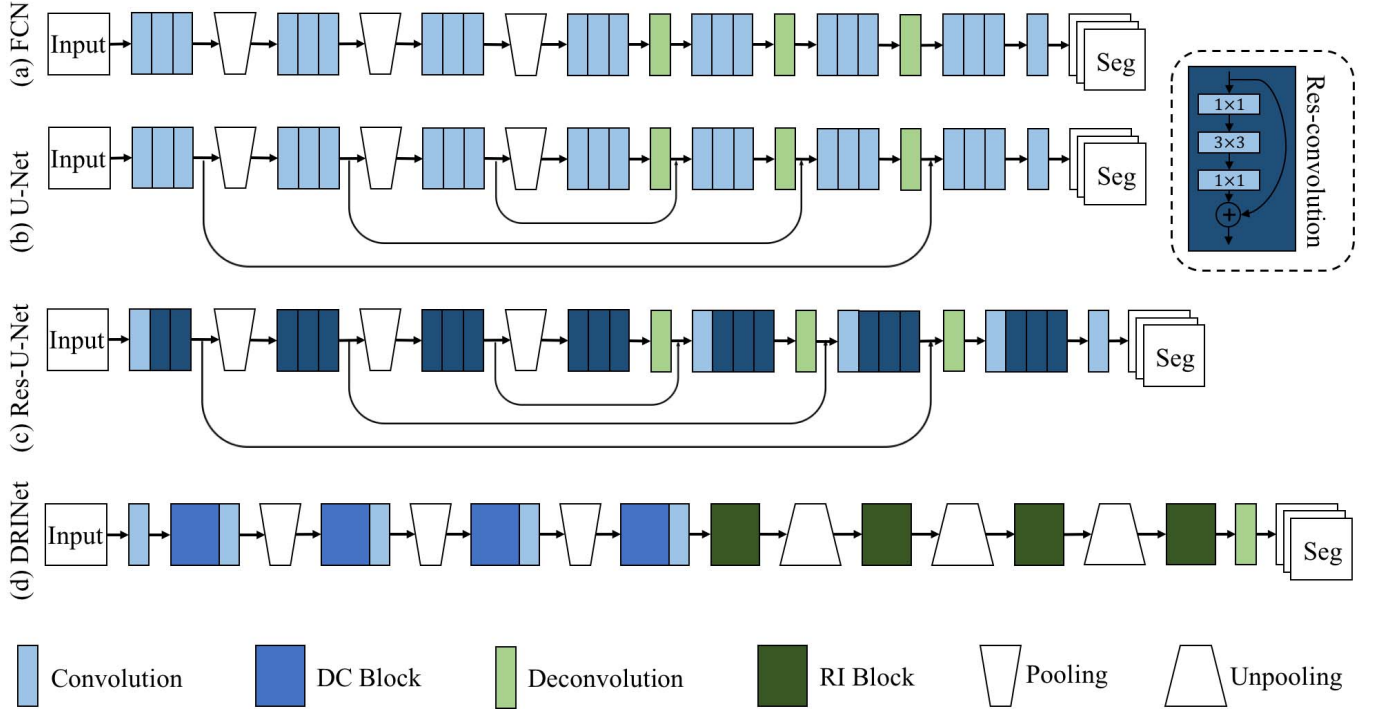
Fig. 2. Overview of the FCN, the U-Net, the Res-U-Net and the DRINet. DC block and RI block represent the dense connection block and the residual Inception block. In the DRINet, the DC, RI, and unpooling blocks are depicted in Fig. 3, 4, and 5, respectively. In the Res-U-Net, the residual convolution means the bottleneck building block used in the ResNet-50/101/152 [11].
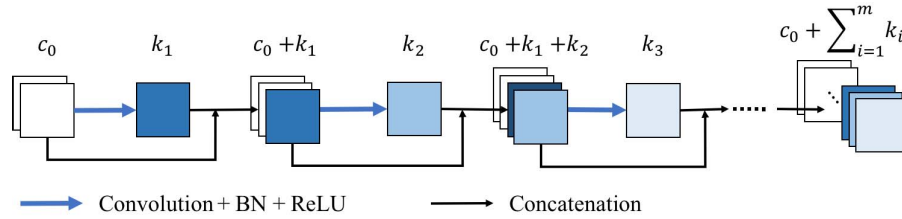

Fig. 3. A dense connection block contains m convolution layers. The output channel number of each convolution layer k_i is the growth rate. BN and ReLU apply on every convolution layer. The input and output of a convolution layer is concatenated so deep supervision is allowed.

rectified linear unit (ReLU). In the standard convolution layer, we have:

$$x_{l+1} = f(x_l) \tag{1}$$

while in the dense connection block [7] we have

$$x_{l+1} = f(x_l) \circ x_l. \tag{2}$$

Here $\circ$ indicates concatenation.

The number of output channels from standard convolution layers are usually fixed and typically 64 or 128. As a result, it is expensive in terms of memory to concatenate the outputs of preceding convolution layers. In addition, the concatenation also leads to many redundant features. Therefore, Huang *et al.* [7] propose to use 1×1 convolutions to reduce the output size. As shown in Fig. 3, within a dense connection block, the size of the output channel for each convolution layer k_i is typically small, e.g. 12 or 24 and this is commonly referred to as the growth rate of the network.

Using dense connection blocks in the analysis path leads to three major advantages: 1) Gradient propagation through

the network is more efficient. Conventionally, it is difficult to ensure that gradients backpropagate to lower layers in the network. Therefore, it is important to use dense connection blocks to alleviate the effect of vanishing gradients. 2) The input to the synthesis path consists of feature maps output from all preceding layers, instead of only the last layer, which reuses the feature maps. 3) It is easy to use the growth rate to control the parameter space, resulting in good network performance. The latter two advantages will be verified in the following experiments.

C. Residual Inception Block

In the synthesis path of the DRINet, we propose to use the residual Inception blocks, which is depicted in Fig. 4. Similar to the original inception modules [10], the idea is to aggregate feature maps from different branches, where the input feature maps are convolved using kernels in different sizes. The residual connections make the learning easier since a residual inception block learns a function with reference to
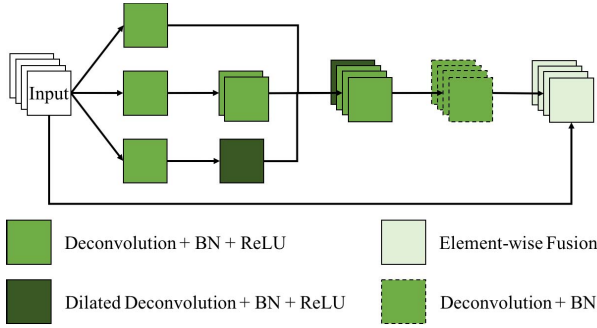
Fig. 4. A residual Inception block is an Inception module with residual connections. An Inception module is a weighted combination of features maps from a few branches. Each branch process the input feature maps using deconvolutions with different kernel sizes.
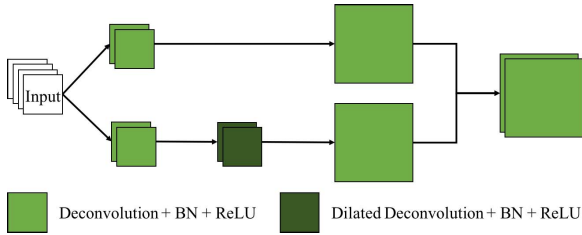

Fig. 5. An unpooling block is a mini Inception module and it upsamples the input feature maps.

the input feature maps, instead of learning an unreferenced function.

In terms of the kernel sizes in convolutions, it is difficult to determine the optimal size for each convolution. In the FCN and the U-Net, the kernel size of convolutions is fixed as 3×3. In the inception module, convolutions of different kernel sizes are used in parallel. In implementation, the feature maps are combined using concatenation and a deconvolution layer with 1×1 kernel learns the combination weights. The deconvolutions are transposed convolutions. In the proposed Inception modules, deconvolutions work the same as the convolutions. The purpose of this is to differentiate with convolutions in the analysis path in symbols.

Unlike the Inception Res-Net [9] having various inception modules, we propose to use identical inception blocks in the DRINet, which is easy to implement. We propose to aggregate feature maps convolved by three kernels, namely 1×1, 3×3, and 5×5. Inspired by the DeepLab [17], the deconvolution with a 5×5 kernel is replaced by a dilated deconvolution with a 3×3 kernel, which is more efficient in memory. To further limit the size of the parameter space, a bottleneck deconvolution is used in each branch.

Formally, let $g(\cdot)$ denotes a deconvolution function followed by BN and ReLU and $g_b(\cdot)$ and $g_d(\cdot)$ represent bottleneck and dilated deconvolution respectively. As a result we obtain

$$x_{l+1} = g_b(g_b(x_l) \circ g(g_b(x_l)) \circ g_d(g_b(x_l))) + x_l. \quad (3)$$

D. Unpooling Block

We propose an unpooling block shown in Fig. 5 to upsample the feature maps in the synthesis path. The unpooling block

can be viewed as a mini inception module, which combines upsampled feature maps from two branches. In each branch, the input feature maps are convolved using kernels in different sizes, namely 1×1 and 5×5. The resulting feature maps are then upsampled using a deconvolution layer with stride 2. Again, the deconvolution with a 5×5 kernel is replaced by a dilated deconvolution with a 3×3 kernel in order to ensure memory efficiency. Also, to limit the parameter space, the input feature maps are firstly convolved by a bottleneck layer in each branch, which is similar to the residual inception block. The combination of upsampled feature maps is achieved via concatenation. Formally, let $g^2(\cdot)$ denotes the deconvolution function with stride 2. The upsampled feature maps are therefore:

$$x_{l+1} = g^2(g_b(x_l)) \circ g^2(g_d(g_b(x_l))). \quad (4)$$

The major advantage of the proposed unpooling block is the aggregation of different upsampled feature maps. Specifically, simply upsampling the input feature maps using a deconvolution layer is likely to produce errors. For instance, a small error in the input feature maps is likely to be enlarged, which finally results in errors in the segmentation results. In contrast, convolving the input feature maps with different kernels leads to different intermediate feature maps. Upsampling these feature maps separately and combining them together reduce the effect of errors.

E. Evaluation Metrics

In multi-class segmentation on brain CSF and abdominal organs, we use the well-known Dice coefficient as well as sensitivity (SE) and precision (PR) for evaluation. In evaluation in the BraTS challenge, we use the same metrics used in the challenge, namely the Dice coefficient, the SE, the specificity (SP), and the Hausdorff95 distance. The Hausdorff95 distance is a robust version of the standard Hausdorff distance, which measures 95 quantile of the distance between two surfaces, instead of the maximum.

F. Implementation Details

In this work, we use cross-entropy as the loss function for all networks. We use the Adam method [18] for optimization with the following parameters: $\beta_1 = 0.9, \beta_2 = 0.999, \epsilon = 1e - 8$. An initial learning rate of $1e - 3$ is utilized. The weights are all initialized from a truncated normal distribution of standard deviation of 0.01. Batch normalization [16] layers are employed in all convolution and deconvolution layers except the last convolution/deconvolution layer. There are three convolution layers in each dense connection block and the kernel size is 3×3 with stride 1. There are three residual inception modules in each residual Inception block. For the standard deconvolution layers in the residual Inception module, the kernel size is 3×3 and the stride is 1. All networks used in this paper are implemented on the Tensorflow[1] platform.

[1]https://www.tensorflow.org/

IV. EXPERIMENTS AND RESULTS

A. CSF Segmentation in CT Images

1) Overview: Assessment of CSF volume, within ventricles and cortical sulci, is important for numerous neurological and neurosurgical applications. In many applications where rapid assessment is required (e.g. stroke), CT is preferred over MRI [19]. A common condition requiring the quantification of CSF is hydrocephalus (ventricular enlargement), a potentially life-threatening, but reversible condition; caused by a wide range of pathologies including hemorrhage, edema or tumors [20]. In these cases, CSF space quantification, especially comparison of ventricular to sulcal compartments, is important for distinguishing hydrocephalus from atrophy (due to age-related ischemia or degeneration) [21]. Standard quantification methods rely upon simple measurement of ventricular spans [22]. However, given the complex ventricular shape, these are imprecise, vary between observers and do not allow for accurate estimation of sulcal CSF [23].

The challenges for multi-class CSF segmentation in CT are three-fold: 1) clinical CT images are often acquired as stacks of 2D image slices with large slice thickness. Thus, each slice is usually separately analyzed, however the position of the patient's head is usually highly variable. Therefore, the CSF on each 2D image slice can vary significantly in terms of its configuration and shape; 2) patients often have background disease (e.g. old infarcts) which can have similar intensities to CSF. 3) at the borders of different categories of CSF, segmentation errors often occur. Many existing methods [24]–[32] are not robust to these problems. To the best of our knowledge, this is the first attempt to solve the multi-class CSF segmentation problem in CT images.

2) Dataset: CT scans from 133 stroke patients were collected from two local hospitals. All clinical CT scans were collected retrospectively from local PACS databases and anonymized before performing research. Ethical approval was obtained from the Imperial College Joint Research Office. The scans were acquired on three types of CT scanners (GE, Siemens, and Toshiba). The thicknesses of image slices range from 1mm to 7mm and the voxel spacing in plane is approximately 0.4×0.4mm. The image size is 512×512. Table I displays the demographic information of the patients.

The training and validation datasets consist of 781 2D image slices randomly chosen from 101 subjects. 500 of these images were used for training and 281 for validation. A separate test set containing 32 subjects was used. The training, validation, and testing datasets were manually annotated by a human expert. The CSF was segmented into three categories: 1) CSF in the ventricles, 2) CSF in the cerebral cortical sulci, fissures, arachnoid cysts, and 3) other CSF spaces, namely: basal and brainstem cisterns, cerebellar sulci, infratentorial arachnoid cysts. For these image slices, a threshold was chosen to obtain a coarse segmentation on the whole CSF and then the expert edited them using the MRICron software.[2] The suprasellar cistern was bisected, such that CSF anterior to a line joining the bilateral anterior most parts of the cerebral peduncles/midbrain

---

[2]https://people.cas.sc.edu/rorden/mricron/index.html

TABLE I
DEMOGRAPHICS OF PATIENTS IN THE CSF SEGMENTATION EXPERIMENT. THE NIHSS IS THE NATIONAL INSTITUTES OF HEALTH STROKE SCORE WHICH MEASURES PATIENTS' FUNCTIONAL SEVERITY ON ADMISSION

Age (years)	mean±std	71 ± 14
	range	28-94
Gender	male %	52.63
NIHSS	mean±std	10 ± 6.03
	range	1-27

---

was classified within the cerebral compartment (reflecting atrophy of medial temporal and orbitofrontal cortices, and including Sylvian cisterns); while CSF posterior to this line (including interpeduncular, crural and ambient cisterns) was classified within the third cisternal compartment.

3) Pre-Processing and Augmentation: In this work, we do not perform resampling on the CT images. This is because the thickness of the clinical CT images is large (up to 7mm) and resampling the images can introduce inaccuracies and interpolation artifacts. In terms of the image intensity normalization, we employed the similar strategy as described in [17]. We normalized CT images on a per slice basis. This means for each slice, background (i.e. air, bone) was excluded and the remaining intensities were normalized to zero mean and unit deviation. We randomly cropped 128×128 patches from the slice to construct the training set. In this way, the training set contains sufficient number of patches. As our CNNs are fully convolutional, in the testing stage, the input can be the entire image slice.

4) Results: We use the FCN, the U-Net, and the Res-U-Net as baselines. The baseline networks are compared to the DRINet with various growth rates. The results are displayed in Table II.

The FCN and the U-Net perform similarly well in terms of Dice. The results suggest that segmenting the CSF in ventricles is relatively easy while segmenting CSF around brainstem is challenging. As depicted in Fig. 6, the CSF around brainstem is likely to be misclassified. In addition, the skip connections in the U-Net do not improve the segmentation results in this case.

Changing the U-Net architecture into the Res-U-Net architecture makes the network deeper and reduces the number of training parameters. According to [11], this change should only marginally influence on the results. However, the Dice score of the CSF around brainstem decreases under the Res-U-Net architecture. This result indicates that reducing parameters is problematic although the network uses the residual connections.

The growth rate is the key hyper-parameter in the DRINet because it controls the network parameter space and performance. Changing the growth rate allows to compare the performance between baseline networks and the DRINets with a similar number of parameters. Table II shows the results evaluating the effects of growth rate. The DRINet with a growth rate of 12 has a similar number of parameters as the Res-U-Net. This DRINet segments the CSF around brainstem significantly better than the Res-U-Net. The DRINet with a

TABLE II
PERFORMANCE COMPARISON AMONG THE BASELINE CNNS AND THE DRINET WITH DIFFERENT GROWTH RATES.
THE NUMBERS UNDER THE DRINET INDICATE THE GROWTH RATES IN EACH DENSE CONNECTION BLOCK

		Dice (%)				SE (%)			PR (%)			# params
		Ventricles	Cortex	Brainstem	Total	Ventricles	Cortex	Brainstem	Ventricles	Cortex	Brainstem	
FCN	val	83.29	76.71	80.74	84.16	90.17	80.06	79.48	93.47	85.13	83.19	2.71M
	test	92.89	89.01	85.25	90.91	92.86	88.50	86.73	94.76	91.18	84.52	
U-Net [5]	val	82.67	76.10	80.45	84.65	90.07	**83.72**	78.50	93.24	82.60	83.28	2.91M
	test	92.45	89.18	85.20	91.03	92.18	**91.70**	85.31	94.44	88.22	85.73	
Res-U-Net	val	81.66	73.99	76.34	84.15	89.72	79.48	75.84	92.84	85.50	81.67	0.96M
	test	91.64	88.73	82.94	90.76	91.54	87.67	82.43	93.81	91.39	84.34	
DRINet 12,12,12,12	val	84.98	76.87	86.72	82.96	87.24	75.47	76.99	**95.87**	**89.49**	**88.71**	0.85M
	test	92.13	87.77	86.08	89.37	88.76	82.78	82.99	**97.52**	**95.75**	90.29	
DRINet 24,24,24,24	val	85.08	**80.70**	90.87	84.44	91.32	79.67	82.57	93.21	87.12	85.58	2.80M
	test	93.84	89.97	88.40	91.27	**94.78**	88.34	**89.55**	94.27	93.23	87.91	
DRINet 36,36,36,36	val	85.00	80.19	90.08	84.67	89.97	81.73	81.18	94.30	85.57	86.71	5.85M
	test	93.70	90.33	88.48	91.52	92.80	90.23	88.22	96.20	91.93	89.45	
DRINet 48,48,48,48	val	**87.39**	80.00	**91.08**	**84.89**	91.06	82.36	82.18	93.59	85.29	86.74	10.03M
	test	**94.28**	**90.64**	**88.96**	**91.85**	94.19	91.00	89.39	95.55	91.74	89.24	
DRINet 64,64,64,64	val	86.97	79.95	90.58	84.62	90.63	80.51	81.15	93.96	86.64	88.33	17.33M
	test	94.15	90.20	**88.96**	91.53	94.27	88.78	87.43	95.37	93.37	**91.28**	
DRINet 12,24,36,48	val	85.74	79.38	87.92	84.55	90.88	81.81	82.21	93.50	85.40	85.21	4.11M
	test	93.87	90.26	88.15	91.50	93.95	90.32	88.91	95.38	91.77	88.15	
DRINet 24,36,48,64	val	86.98	79.63	90.84	84.69	**93.90**	**85.75**	**87.32**	90.74	81.58	81.30	8.03M
	test	94.27	90.16	88.82	91.51	94.19	89.53	87.83	95.68	92.45	90.53	
DRINet 36,48,64,80	val	86.45	80.08	89.68	84.72	89.86	80.96	82.10	94.58	86.43	87.22	13.70M
	test	93.76	90.27	88.82	91.46	92.44	89.38	88.59	96.64	92.79	89.76	

growth rate 24 is comparable to the FCN and the U-Net in terms of the size of parameter space. It performs better than the FCN and the U-Net in terms of the CSF in ventricles and around brainstem. If the growth rate increases to 48, the DRINet performs best in all three parts of the CSF segmentation, as well as the whole CSF segmentation. When the growth rate becomes very large (e.g. 64), the DRINet is likely to overfit and the performance decreases. In the following experiments, a growth rate of 48 is used.

Huang *et al.* [8] noted that a larger growth rate in the higher layers is beneficial for the performance of network. In our experiments, we evaluate this strategy using growth rates like 12, 24, 36, 48 in each dense connection block. Comparing DRINets using identical growth rate and increasing growth rates, which have similar number of parameters, the DRINets using increasing growth rates do not perform significantly better in any part of CSF segmentations.

5) Run Time: Pre-processing was performed on a desktop PC with an Core i7-3770 processor and 32GB RAM. CNNs were trained and tested on an NVIDIA TITAN XP GPU processor except for the DRINets with large growth rates (e.g. 48, 64), which were trained on two GPUs to keep the batch size sufficiently large. On average it took 44.46s for the DRINet to segment the CSF in one image. The training time of the DRINet with the best performance was 21.37 hours. In contrast, the U-Net is faster with 11.44 hours for training and 23.56s per image for testing. Although the DRINet is slower, its run time is acceptable.

B. Multi-Organ Segmentation

1) Overview: Segmenting abdominal organs is important for clinical diagnosis and surgery planning [33]. There are two major challenges in the multi-organ segmentation problem:

1) Abdominal organs are highly deformable and mobile and therefore can have various shapes and sizes; 2) the contrast between organs is often poor making it difficult to identify boundaries between organs.

Abdominal organ segmentation is a popular topic for which many solutions have been proposed. Many methods were based on statistical shape models [34] or multi-atlas segmentation [34]–[38]. Using recent deep learning approaches, the segmentation accuracy has significantly improved, particularly for smaller organs (e.g. pancreas). Furthermore, deep learning approaches are much faster than conventional methods [4], [39], [40].

2) Dataset: 3D abdominal CT scans were used in this experiment to evaluate the performance of the DRINet. Image acquisition parameters and patient demographics for the dataset used here can be found in [37].

Pre-processing and augmentation were carried out in similar manner to those for CSF segmentation. The only difference is that in the CSF segmentation, the image intensity normalization is performed per slice while in this multi-organ segmentation task, the image intensity is normalized per volume. The 128×128 image patches were randomly cropped to develop the training set.

We used the same the experimental settings and CNN configurations as in the previous experiments, so no parameters tuning is performed in this experiment. The purpose is to validate the flexibility of the DRINet. Therefore, we only split the whole dataset into a training set (75 subjects) and a separate testing set (75 subjects).

3) Baseline: Again, the U-Net and the Res-U-Net are used as baselines. Table III displays the segmentation results. The performance of the U-Net and the Res-U-Net is comparable. The Res-U-Net provides better PR but worse SE than the U-Net in segmenting the pancreas and kidneys. As mentioned
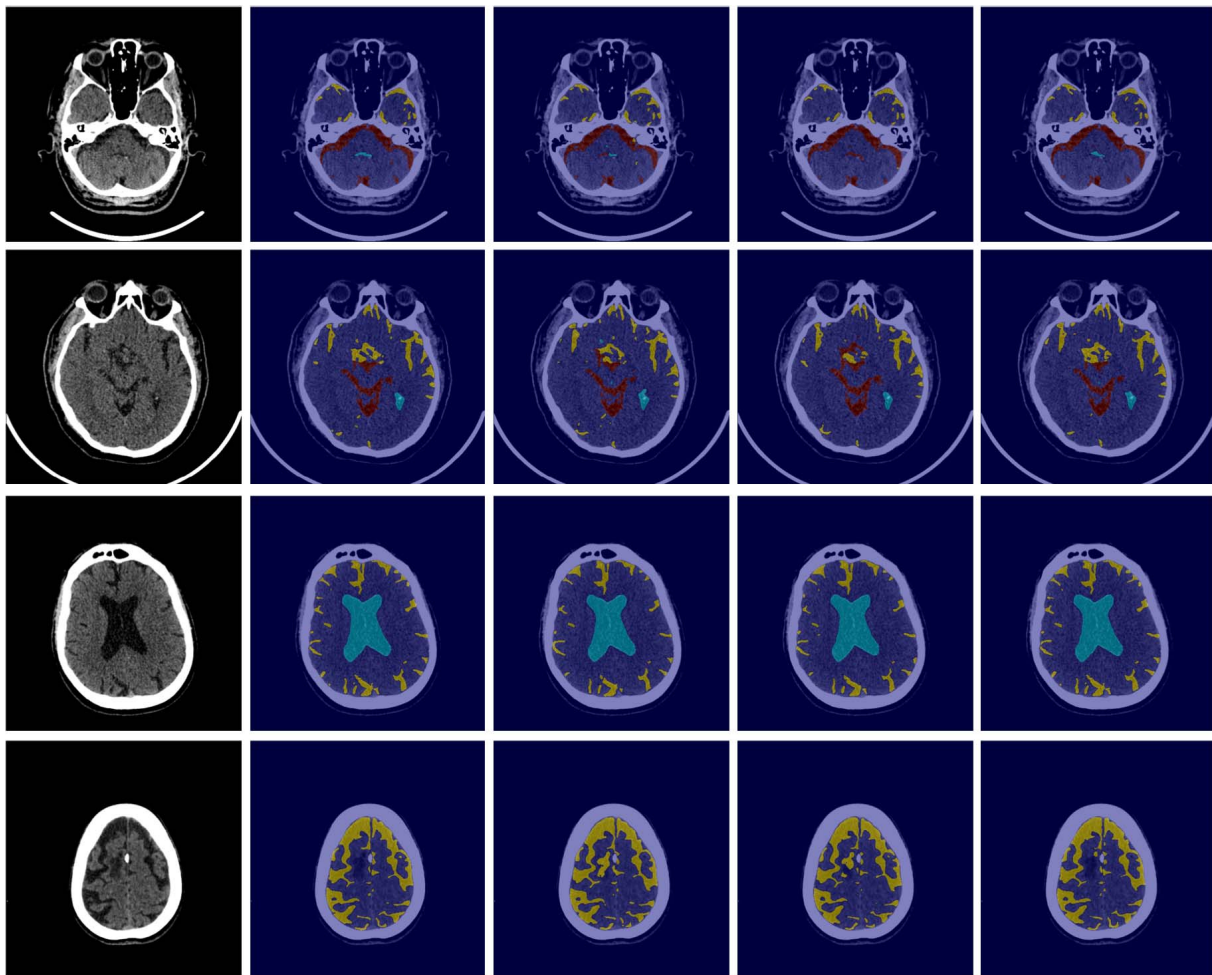
Fig. 6. The visual examples of multi-class CSF segmentations. The first column displays the original images. The second column shows the manual references. The following columns demonstrate the segmentations of the U-Net, the Res-U-Net, and the DRINet.

TABLE III

PERFORMANCE COMPARISON AMONG THE U-NET, THE RES-U-NET AND THE DRINET. THE DRINET OUTPERFORMED THE BASELINE CNNS, PARTICULARLY IN TERMS OF THE PANCREAS

	Dice (%)				SE (%)				PR (%)			
	Pancreas	Kidneys	Liver	Spleen	Pancreas	Kidneys	Liver	Spleen	Pancreas	Kidneys	Liver	Spleen
U-Net [5]	80.09	95.80	94.70	94.72	74.89	**95.86**	92.79	93.13	87.98	95.85	**96.65**	95.98
Res-U-Net	79.09	95.41	96.20	94.71	72.41	93.72	96.15	92.92	**89.49**	**97.28**	96.26	95.94
DRINet	**83.42**	**95.96**	**96.57**	**95.64**	**80.29**	95.84	**96.69**	**95.63**	87.95	96.20	96.47	**96.13**

above, the pancreas is the most challenging organ to segment because of its thin and various structure. The strength of the proposed DRINet is demonstrated by the fact that it is able to segment the challenging organs significantly better than the baseline CNNs approaches.

4) Comparison With Existing Methods: We compare the DRINet with existing methods evaluated on the same dataset. References [36] and [37] proposed methods based on conventional machine learning approaches. According to the results (displayed in Table IV) they have achieved fairly good segmentations in terms of kidneys, liver, and spleen. The method proposed by Tong *et al.* [37] is much faster than the one proposed by Wolz *et al.* [36]. The 3D FCN proposed by Roth *et al.* [4] is the state-of-the-art method based on deep CNNs. It is clear that the 3D FCN achieves significantly better results in the pancreas segmentation. Furthermore the inference time

is significantly reduced. However, in terms of the other organs, namely the kidneys, liver, and spleen, the 3D FCN did not offer significant improvements.

The DRINet outperforms the 3D FCN achieving the state-of-the-art based on this dataset. Specifically, it improves the pancreas segmentation further from the 3D FCN. In addition, the DRINet promotes the segmentation on other organs as well. Note that the DRINet is only based on 2D image slices without using 3D contextual information. Therefore, this experiments verifies the DRINet is powerful and robust in the multi-organ segmentation problem.

C. Brain Tumor Segmentation

1) Overview: Brain tumors are routinely diagnosed using multi-modal MRI, including native T1-weighted (T1), post-contrast T1-weighted (T1-Gd), T2-weighted (T2), and T2 fluid
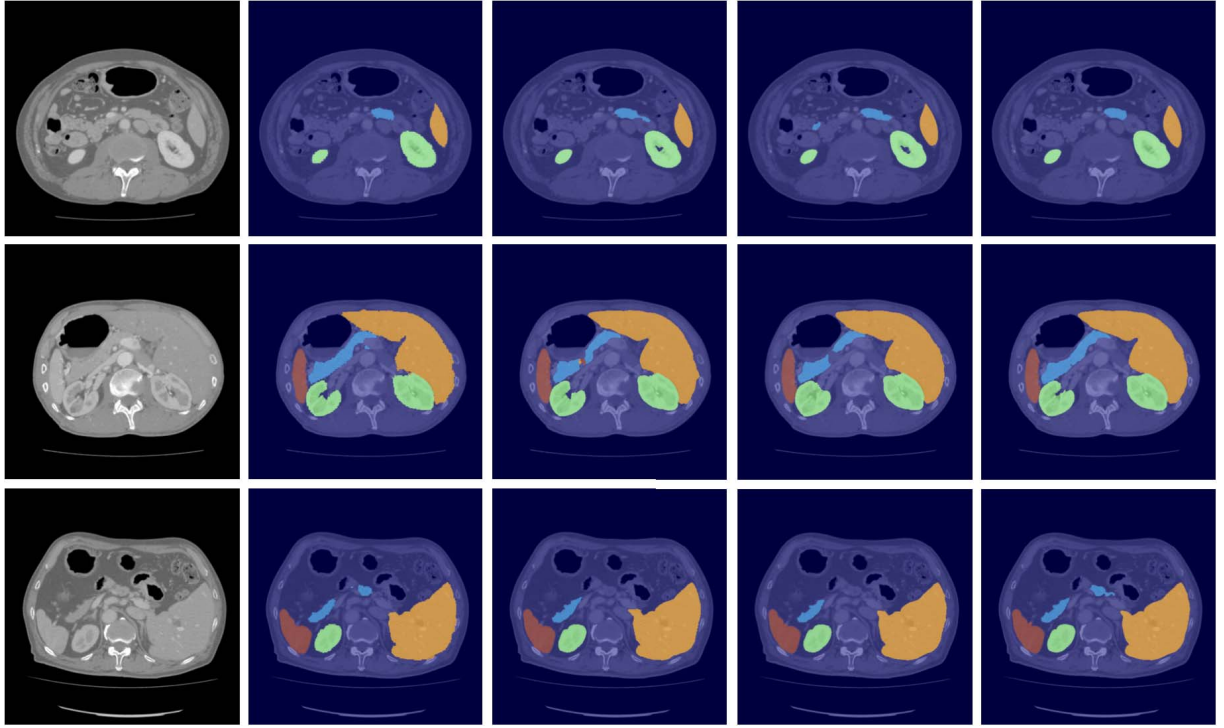
Fig. 7.   The visual examples of abdominal multi-organ segmentations. The first column displays the original images. The second column shows the manual references. The following columns demonstrate the segmentations of the U-Net, the Res-U-Net, and the DRINet.

TABLE IV

PERFORMANCE COMPARISON AMONG DIFFERENT ALGORITHMS. IT IS CLEAR THAT THE DRINET IS SUPERIOR TO THE EXISTING METHODS

	Dice (%)				Time (h)
	Pancreas	Kidneys	Liver	Spleen	
Wolz et al. [36]	69.60	92.50	94.00	92.00	51
Tong et al. [37]	69.80	93.40	94.90	91.90	0.5
Roth et al. [4]	82.20	-	95.40	92.80	0.07
DRINet	**83.42**	**95.96**	**96.57**	**95.64**	**0.02**

attenuated inversion recovery (FLAIR) image sequences [41]. Quantification of the tumors based on the multi-modal MRI benefits the diagnosis and treatment [42]. Segmenting tumors into necrotic and non-enhancing tumors, the peritumoral edema, and gadolinium enhancing tumors has been a popular research topic [43].

2) Dataset: We propose to use the training dataset of the BraTS 2017 challenge. There are 285 subjects in total and we randomly select 50 for training and the remaining 235 ones for testing. The segmentation is based on 2D patches of size of 64×64. Since the training patch size is smaller compared to that in the previous experiments, all CNNs in this experiments have two downsampling and upsampling process and all the other network configurations are fixed. According to [43], the images have been preprocessed: images were co-registered into the same anatomical template; skulls were stripped; voxels were resampled to isotropic resolution ($1 \ mm^3$). We normalize the image intensities into zero mean and unit deviation. No post-processing trick is used in any case. The evaluation is based on the whole tumor region,

the tumor core region, and the enhancing tumor core region, instead of individual tumor structures.

3) Results: On this benchmark dataset, we evaluate the three key components of the DRINet: the dense connection block, the residual Inception block, and the unpooling block. We set the FCN as the baseline CNN and separately add one of the proposed blocks to verify its contribution. We also compare their performance with the U-Net and the DRINet.

Table V shows the results: In terms of the whole tumor structure, the added blocks do not affect the Dice scores significantly. The dense connection block and the residual Inception block increase the sensitivity and the Hausdorff distances and decrease the specificity, which means they increase the number of false positives (FPs). In contrast, the unpooling block decreases the sensitivity and Hausdorff distance and increases the specificity, which means it reduces FPs but introduces FNs. Combining them together results in a trade-off between FNs and FPs. Therefore, the overall performance increases.

In terms of the tumor core and enhanced core, the three blocks increase the Dice scores and specificity while decreasing their sensitivity and Hausdorff distances. This means the overall performance for the segmentation of the tumor core and the enhanced core is improved. However, since their sizes are fairly small, some FNs occur.

The DRINet with three powerful blocks achieves better segmentation results than the U-Net in terms of the dice scores, the sensitivity, and the Hausdorff distances. Regarding the Res-U-Net, since the parameter space is small, it cannot perform as well as the U-Net in this case. Fig. 8 shows that the training error of the Res-U-Net is larger than that of the U-Net and the DRINet. Therefore, the Dice coefficients given by the

TABLE V
THE SEGMENTATION RESULTS OF DIFFERENT NETWORKS. THE ENTRIES IN BOLD HIGHLIGHT THE BEST COMPARABLE RESULTS

| Network	Dice (%)			SE (%)			SP (%)			Hausdorff95 (mm)		
	Whole	Core	Enh.	Whole	Core	Enh.	Whole	Core	Enh.	Whole	Core	Enh.
U-Net [5]	81.51	71.30	63.05	81.69	72.51	79.70	99.86	99.92	99.94	42.07	34.44	36.46
Res-U-Net	71.50	67.75	60.06	60.25	66.06	68.27	**99.97**	99.93	**99.97**	**21.98**	**25.00**	27.56
FCN	81.42	70.4	61.49	80.84	**77.12**	**80.76**	99.85	99.80	99.92	42.19	47.24	44.08
FCN+dense	81.09	71.98	63.29	84.90	74.81	78.56	99.80	99.91	99.95	48.34	39.36	36.56
FCN+RI	81.89	72.30	63.25	**85.26**	74.29	78.02	99.82	99.91	99.95	47.38	36.49	33.97
FCN+unpool	81.81	71.43	63.93	78.56	70.53	75.80	99.91	**99.94**	99.96	33.37	28.39	**27.12**
DRINet	**83.47**	**73.21**	**64.98**	84.53	74.93	80.35	99.86	99.92	99.94	36.4	25.59	30.31
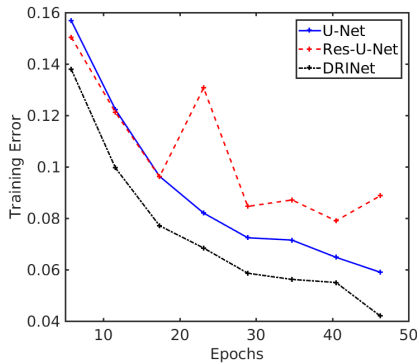
Fig. 8. The training error comparisons among different CNNs.

Res-U-Net on tumors are the worst among all the CNNs. According to the low sensitivity, the high specificity, and the low Hausdorff distance, it is clear that the segmentation results by the Res-U-Net have many FNs but few FPs.

V. DISCUSSION AND CONCLUSION

In this paper, a novel CNN architecture, DRINet, is proposed. The DRINet has three key features, namely the use of dense connection blocks, residual inception blocks, and the unpooling blocks. These blocks deepen and widen the network significantly and the parameter space can be controlled via the growth rate. The gradient propagation is improved due to the dense connections and residual connections. As a result, the performance of the DRINet is significantly improved when compared to the standard U-Net. In addition, the DRINet architecture is highly flexible: Within a block, the convolution/deconvolution layers can be changed adaptively. It is therefore easy to integrate the blocks into other CNN architectures.

In this paper, we focus on evaluating the performance of the proposed DRINet and each of its components. The segmentation results of each problem can be improved using some domain knowledge and post-processing. For instance, in the brain CSF segmentation problem, a brain mask could be added. In the abdominal organ segmentation task, 3D contextual information could be included. In the BraTS problem, the CRF model could be used to remove FPs.

Among the three experiments, the multi-class CSF segmentation on CT images is novel. To the best of our knowledge, we are the first to attempt on this problem and the proposed DRINet results in good segmentation. In the future, we plan

extend the proposed approach to segment lesions as well as CSF using a single DRINet. This is useful in clinical settings for prognostication after stroke [44] or estimating cerebral hemorrhage risk [45], [46].

In the context of abdominal multi-organ segmentation, the DRINet achieves very good results although the segmentation is based on 2D CT image slices. Our results show that the DRINet improves the segmentation on small and various organs like pancreas as well as big organs like liver. It is of interest to extend its ability to segment more challenging organs such as arteries and veins, which could make the DRINet more useful in clinics.

A limitation of the DRINet approach is that the increase of the growth rate results in many more parameters, which may lead the training more difficult and testing slower. In the future, the research could focus on simplifying the network structure while maintaining its ability.

REFERENCES

[1] H. Greenspan, B. V. Ginneken, and R. M. Summers, "Guest editorial deep learning in medical imaging: Overview and future promise of an exciting new technique," *IEEE Trans. Med. Imag.*, vol. 35, no. 5, pp. 1153–1159, Mar. 2016.

[2] A. De Brébisson and G. Montana, "Deep neural networks for anatomical brain segmentation," in *Proc. CVPR Workshops*, Jun. 2015, pp. 20–28.

[3] M. R. Avendi, A. Kheradvar, and H. Jafarkhani, "A combined deep-learning and deformable-model approach to fully automatic segmentation of the left ventricle in cardiac MRI," *Med. Image Anal.*, vol. 30, pp. 108–119, May 2016.

[4] H. R. Roth *et al.* (Apr. 2017). "Hierarchical 3D fully convolutional networks for multi-organ segmentation." [Online]. Available: https://arxiv.org/abs/1704.06382

[5] O. Ronneberger, P. Fischer, and T. Brox, "U-net: Convolutional networks for biomedical image segmentation," in *Proc. MICCAI*, Nov. 2015, pp. 234–241.

[6] Ö. Çiçek, A. Abdulkadir, S. S. Lienkamp, T. Brox, and O. Ronneberger, "3D U-net: Learning dense volumetric segmentation from sparse annotation," in *Proc. MICCAI*, Jun. 2016, pp. 424–432.

[7] G. Huang, Z. Liu, L. Van Der Maaten, and K. Q. Weinberger, "Densely connected convolutional networks," in *Proc. CVPR*, Aug. 2016, pp. 4700–4708.

[8] G. Huang, D. Chen, T. Li, F. Wu, L. Van Der Maaten, and K. Q. Weinberger, "Multi-scale dense convolutional networks for efficient prediction," in *Proc. ICLR*, 2018.

[9] C. Szegedy, S. Ioffe, V. Vanhoucke, and A. Alemi, "Inception-v4, inception-resnet and the impact of residual connections on learning," in *Proc. AAAI*, 2017, pp. 4278–4284.

[10] C. Szegedy *et al.*, "Going deeper with convolutions," in *Proc. CVPR*, Jun. 2015, pp. 1–9.

[11] K. He, X. Zhang, S. Ren, and J. Sun, "Deep residual learning for image recognition," in *Proc. CVPR*, Jun. 2016, pp. 770–778.

[12] L.-C. Chen, G. Papandreou, I. Kokkinos, K. Murphy, and A. L. Yuille, "DeepLab: Semantic image segmentation with deep convolutional nets, atrous convolution, and fully connected CRFs," *IEEE Trans. Pattern Anal. Mach. Intell.*, vol. 40, no. 4, pp. 834–848, Apr. 2018.

[13] L.-C. Chen, G. Papandreou, F. Schroff, and H. Adam. (Jun. 2017). "Rethinking atrous convolution for semantic image segmentation." [Online]. Available: https://arxiv.org/abs/1706.05587

[14] S. Jégou, M. Drozdzal, D. Vazquez, A. Romero, and Y. Bengio, "The one hundred layers tiramisu: Fully convolutional densenets for semantic segmentation," in *Proc. CVPR Workshops*, Jul. 2017, pp. 1175–1183.

[15] H. Zhao, J. Shi, X. Qi, X. Wang, and J. Jia, "Pyramid scene parsing network," in *Proc. CVPR*, Jul. 2017, pp. 2881–2890.

[16] S. Ioffe and C. Szegedy, "Batch normalization: Accelerating deep network training by reducing internal covariate shift," in *Proc. ICML*, Feb. 2015, pp. 448–456.

[17] L. Chen, P. Bentley, and D. Rueckert, "Fully automatic acute ischemic lesion segmentation in DWI using convolutional neural networks," *NeuroImage: Clin.*, vol. 15, pp. 633–643, Jun. 2017.

[18] D. P. Kingma and J. Ba, "Adam: A method for stochastic optimization," in *Proc. ICLR*, 2015.

[19] N. Sanossian *et al.*, "Utilization of emergent neuroimaging for thrombolysis-eligible stroke patients," *J. Neuroimag.*, vol. 27, no. 1, pp. 59–64, 2017.

[20] L. Pople, "Hydrocephalus and shunts: What the neurologist should know," *J. Neurol., Neurosurgery Psychiatry*, vol. 73, no. 1, pp. I17–I22, 2002.

[21] M. A. Williams and N. R. Relkin, "Diagnosis and management of idiopathic normal-pressure hydrocephalus," *Neurol., Clin. Pract.*, vol. 3, no. 5, pp. 375–385, 2013.

[22] A. V. Kulkarni, J. M. Drake, D. C. Armstrong, and P. B. Dirks, "Measurement of ventricular size: Reliability of the frontal and occipital horn ratio compared to subjective assessment," *Pediatric Neurosurgery*, vol. 31, no. 2, pp. 65–70, 1999.

[23] F. Pasquier, D. Leys, J. G. Weerts, F. Mounier-Vehier, F. Barkhof, and P. Scheltens, "Inter- and intraobserver reproducibility of cerebral atrophy assessment on MRI scans with hemispheric infarcts," *Eur. Neurol.*, vol. 36, no. 5, pp. 268–272, 1996.

[24] T. Sandor, D. Metcalf, and Y.-J. Kim, "Segmentation of brain CT images using the concept of region growing," *Int. J. Bio-Med. Comput.*, vol. 29, no. 2, pp. 133–147, 1991.

[25] U. E. Ruttimann, E. M. Joyce, D. E. Rio, and M. J. Eckardt, "Fully automated segmentation of cerebrospinal fluid in computed tomography," *Psychiatry Res., Neuroimag.*, vol. 50, no. 2, pp. 101–119, 1993.

[26] T. H. Lee, M. F. A. Fauzi, and R. Komiya, "Segmentation of CT brain images using K-means and EM clustering," in *Proc. 5th Int. Conf. Comput. Graph., Imag. Vis.*, Aug. 2008, pp. 339–344.

[27] T. H. Lee, M. F. A. Fauzi, and R. Komiya, "Segmentation of CT brain images using unsupervised clusterings," *J. Vis.*, vol. 12, no. 2, pp. 131–138, 2009.

[28] W. Chen and K. Najarian, "Segmentation of ventricles in brain CT images using gaussian mixture model method," in *Proc. Int. Conf. Complex Med. Eng.*, Apr. 2009, pp. 1–6.

[29] V. Gupta *et al.*, "Automatic segmentation of cerebrospinal fluid, white and gray matter in unenhanced computed tomography images," *Acad. Radiol.*, vol. 17, no. 11, pp. 1350–1358, 2010.

[30] L. E. Poh, V. Gupta, A. Johnson, R. Kazmierski, and W. L. Nowinski, "Automatic segmentation of ventricular cerebrospinal fluid from ischemic stroke CT images," *Neuroinformatics*, vol. 10, no. 2, pp. 159–172, 2012.

[31] X. Qian, J. Wang, S. Guo, and Q. Li, "An active contour model for medical image segmentation with application to brain CT image," *Med. Phys.*, vol. 40, no. 2, p. 021911, 2013.

[32] X. Qian, Y. Lin, Y. Zhao, X. Yue, B. Lu, and J. Wang, "Objective ventricle segmentation in brain CT with ischemic stroke based on anatomical knowledge," *BioMed Res. Int.*, vol. 2017, Feb. 2017, Art. no. 8690892.

[33] M. G. Linguraru, J. A. Pura, V. Pamulapati, and R. M. Summers, "Statistical 4D graphs for multi-organ abdominal segmentation from multiphase CT," *Med. Image Anal.*, vol. 16, no. 4, pp. 904–914, 2012.

[34] T. Okada *et al.*, "Automated segmentation of the liver from 3D CT images using probabilistic atlas and multilevel statistical shape model," *Acad. Radiol.*, vol. 15, no. 11, pp. 1390–1403, 2008.

[35] Z. Wang *et al.*, "Geodesic patch-based segmentation," in *Proc. MICCAI*, 2014, pp. 666–673.

[36] R. Wolz, C. Chu, K. Misawa, M. Fujiwara, K. Mori, and D. Rueckert, "Automated abdominal multi-organ segmentation with subject-specific atlas generation," *IEEE Trans. Med. Imag.*, vol. 32, no. 9, pp. 1723–1730, Sep. 2013.

[37] T. Tong *et al.*, "Discriminative dictionary learning for abdominal multi-organ segmentation," *Med. Image Anal.*, vol. 23, no. 1, pp. 92–104, 2015.

[38] C. Chu *et al.*, "Multi-organ segmentation based on spatially-divided probabilistic atlas from 3D abdominal CT images," in *Proc. MICCAI*, 2013, pp. 165–172.

[39] H. R. Roth *et al.* (Jan. 2017). "Spatial aggregation of holistically-nested convolutional neural networks for automated pancreas localization and segmentation." [Online]. Available: https://arxiv.org/abs/1702.00045

[40] J. Cai, L. Lu, Y. Xie, F. Xing, and L. Yang. (Jul. 2017). "Improving deep pancreas segmentation in CT and MRI images via recurrent neural contextual learning and direct loss function." [Online]. Available: https://arxiv.org/abs/1707.04912

[41] S. Bakas *et al.*, "Advancing The Cancer Genome Atlas glioma MRI collections with expert segmentation labels and radiomic features," *Sci. Data*, vol. 4, p. 170117, Sep. 2017.

[42] S. Bakas *et al.*, "Segmentation labels and radiomic features for the pre-operative scans of the TCGA-LGG collection," *Cancer Imag. Arch.*, 2017.

[43] B. H. Menze *et al.*, "The multimodal brain tumor image segmentation benchmark (BRATS)," *IEEE Trans. Med. Imag.*, vol. 34, no. 10, pp. 1993–2024, Oct. 2015.

[44] The IST-3 Collaborative Group, "Association between brain imaging signs, early and late outcomes, and response to intravenous alteplase after acute ischaemic stroke in the third international stroke trial (IST-3): Secondary analysis of a randomised controlled trial," *Lancet Neurol.*, vol. 14, no. 5, pp. 485–496, 2015.

[45] P. Fotiadis *et al.*, "Cortical atrophy in patients with cerebral amyloid angiopathy: A case-control study," *Lancet Neurolo.*, vol. 15, no. 8, pp. 811–819, 2016.

[46] C. M. Dunham, D. A. Hoffman, G. S. Huang, L. A. Omert, D. J. Gemmel, and R. Merrell, "Traumatic intracranial hemorrhage correlates with preinjury brain atrophy, but not with antithrombotic agent use: A retrospective study," *PLoS ONE*, vol. 9, no. 10, p. e109473, 2014.